ACS Infectious Diseases

Open Access

pubs.acs.org/journal/aidcbc

Article

Exploring the Pyrimidine Scaffold for the Development of SARS-CoV-2 M^{pro} Inhibitors

Salvatore Nieddu,◆ Giuseppe Ruggieri,◆ Riccardo De Santis,◆ Paolo Malune, Elisa Patacchini, Valentina Noemi Madia, Francesco Saccoliti, Antonella Messore, Laura Zarbo, Angela Corona, Donatella Amatore, Giorgia Grilli, Alessandra Amoroso, Florigio Lista, Enzo Tramontano, Roberta Costi,* Roberto Di Santo,◆ and Francesca Esposito◆

Cite This: https://doi.org/10.1021/acsinfecdis.6c00583

Read Online

ACCESS | Metrics & More | Article Recommendations | Supporting Information

ABSTRACT: Severe acute respiratory syndrome coronavirus 2 (SARS-CoV-2) is still a major public health issue, even today. Among the SARS-CoV-2 nonstructural proteins, the main protease (M^{pro}) plays a critical role in viral polyprotein processing and is therefore indispensable for viral replication. For this reason, it represents one of the most promising therapeutic targets for the development of antiviral agents against SARS-CoV-2. Currently, only one protease antiviral agent (nirmatrelvir) has received emergency approval for COVID-19 treatment, the disease caused by SARS-CoV-2 infection. However, the emergence of viral mutations may compromise its efficacy, highlighting the urgent need to develop new, safe, and effective protease antiviral agents. In the present work, we designed and synthesized new SARS-CoV-2 M^{pro} small-molecule inhibitors endowed with a pyrimidine scaffold. A series of derivatives were evaluated in both biochemical and cell-based assays to assess their antiviral efficacy, with some of them being able to inhibit the SARS-CoV-2 M^{pro} activity and to suppress viral replication. Docking studies were confirmed by site-directed mutagenesis, and the mechanism of action of the most promising compound was elucidated.

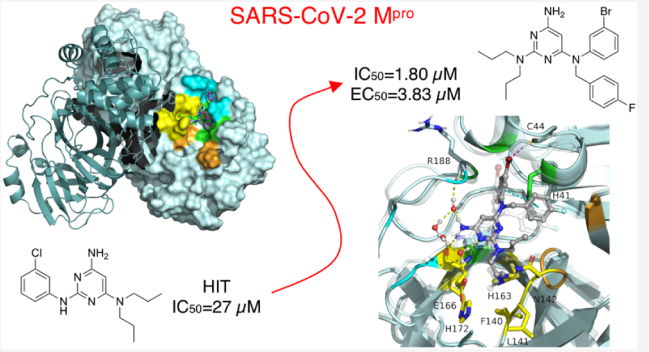

KEYWORDS: *SARS-CoV-2, COVID-19, main protease, pyrimidine derivatives, small molecules, drug design*

INTRODUCTION

Coronaviruses are respiratory pathogens that infect humans and a broad range of animal hosts.[1,2] Among RNA viruses, SARS-CoV-2 harbors one of the largest genomes (~29.9 kb)[3,4] and after infection, translation of ORF1a/b produces the polyproteins pp1a and pp1ab, which are proteolytically processed into 16 nonstructural proteins (nsps) by the viral proteases nsp3 (Papain-like protease, PL^{pro}) and nsp5 (Main protease, M^{pro}).[1]

M^{pro} is a 3C-like protease that serves as the main proteolytic enzyme, cleaving the viral polyprotein at 11 conserved sites to generate nsps 4−16.[5] Structurally, the protein adopts a homodimeric arrangement, with each protomer comprising three domains: domains I and II form a chymotrypsin-like β-barrel architecture harboring the catalytic dyad Cys145−His41, while domain III mediates dimerization, which is essential for enzymatic activity. The active site is organized into five subsites (*S1*−*S5*) that define substrate recognition and binding.[6] Notably, M^{pro} is highly conserved across coronaviruses; indeed, the SARS-CoV-2 enzyme shares sequence identity with the M^{pro} of SARS-CoV (96.1%) and MERS-CoV (~50%). This suggests that inhibitors developed against earlier coronaviruses may retain cross-inhibitory activity.[7,8]

M^{pro} inhibitors can be broadly classified into two categories: covalent (peptidomimetic or nonpeptidomimetic) and noncovalent (orthosteric or allosteric) agents.[9−13] Covalent inhibitors typically exploit electrophilic warheads to target the catalytic cysteine, often achieving a high potency and prolonged target engagement. Representative examples include GC376, a dipeptidyl bisulfite adduct originally developed for feline coronavirus, and its related analogues, which have demonstrated robust antiviral activity in preclinical models.[11] More recently, reversible covalent inhibitors such as nirmatrelvir[14] (**1**, Figure 1) and simnotrelvir[15] (**2**) have been successfully translated into clinical use.

Received: June 12, 2026
Revised: July 27, 2026
Accepted: July 29, 2026

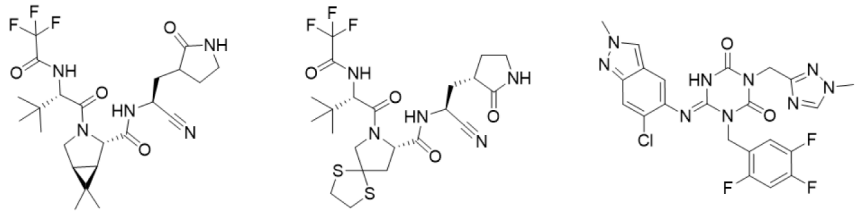

Figure 1. Clinically approved M^{pro} inhibitors **1**−**3**.

Chart 1. Chemical Structures of Hit 4 and Newly Designed 2,4,6-Triaminopyrimidine Derivatives 5a−d,h,i, 6a−g, 7, 8a−c, 9d−g, and 10a,b

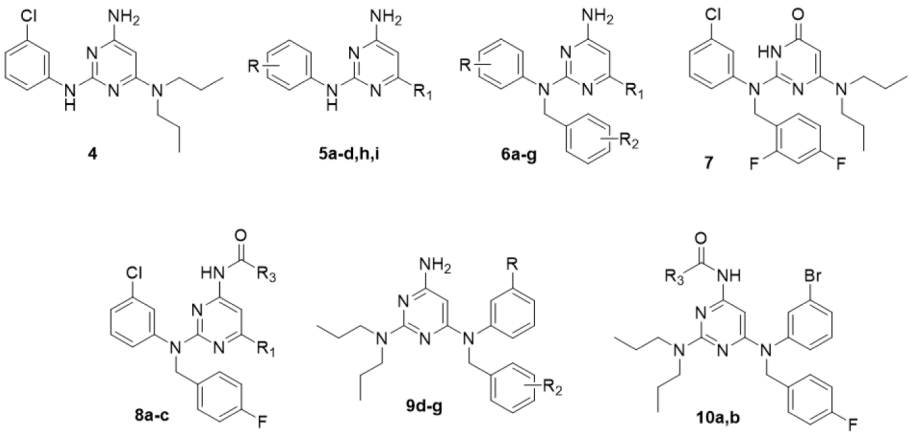

In parallel, noncovalent inhibitors have emerged as an attractive alternative, offering the potential for improved selectivity and reduced risk of off-target reactivity. Structurally diverse scaffolds have been reported, although their optimization has frequently been limited by suboptimal potency, pharmacokinetic liabilities, or susceptibility to resistance.[10,16,17] Among these, ensitrelvir (**3**) represents a notable example of a clinically advanced noncovalent M^{pro} inhibitor, exhibiting potent antiviral activity and favorable oral bioavailability. Similarly, ibuzatrelvir[18] has shown promising preclinical and early clinical profiles, further supporting the viability of this class.

Despite these advances, only nirmatrelvir, administered in combination with ritonavir as Paxlovid,[19] has received regulatory approval to date from the U.S. Food and Drug Administration (FDA), highlighting both the progress achieved and the remaining challenges in the development of M^{pro}-targeting antivirals. Nirmatrelvir is also most effective when initiated within 5 days of symptom onset,[20] and coadministration with ritonavir introduces a significant risk of drug−drug interactions due to potent CYP3A4 inhibition, potentially altering the pharmacokinetics of commonly prescribed medications[21] and limiting the population eligible for therapy. In contrast, ensitrelvir avoids pharmacokinetic boosting but is currently limited by less extensive clinical validation, moderate efficacy, and restricted global availability, and both agents are susceptible to resistance associated with emerging viral variants.[22] Other approved antivirals, including remdesivir and molnupiravir, target the viral polymerase but are limited by modest efficacy, intravenous administration requirements, or less favorable benefit-risk profiles.[23] Collectively, these efforts underscore the continued interest in both covalent and noncovalent strategies to identify next-generation M^{pro} inhibitors with improved efficacy, safety, and resistance profiles.

In this work, we explored the potential of a pyrimidine-based scaffold as a novel chemotype for the inhibition of SARS-CoV-2 M^{pro}. Building on our expertise in antiviral drug design and our recent efforts in the development of anti-SARS-CoV-2 agents,[24−28] we screened our in-house heterocyclic library,[24−30] identifying a 2,4,6-triaminopyrimidine core as a suitable starting point for further optimization.[30]

A focused series of derivatives was designed, synthesized, and evaluated both in biochemical and cell-based assays to assess their antiviral efficacy. Some of them were able to inhibit the SARS-CoV-2 M^{pro} with half-maximal inhibitory concentrations (IC_{50}) in the low micromolar range, showing also the ability to suppress viral replication in cell culture. In addition, a rationalization of the interaction with the biological target has been proposed, based on docking studies and validated by site-directed mutagenesis.

RESULTS AND DISCUSSION

Identification of Pyrimidine Derivatives as Novel M^{pro} Inhibitors

From our in vitro screening, compound **4** (Chart 1) emerged as a promising hit, exhibiting inhibitory activity against SARS-CoV-2 M^{pro} (IC_{50} = 27.00 ± 3.00 μM) and suppressing viral replication by 99.47% at 25 μM (data not shown), without detectable cytotoxicity up to 100 μM.

Kinetic studies identified compound **4** as a mixed inhibitor of SARS-CoV-2 M^{pro} (data not shown), indicating that, in addition to binding the orthosteric pocket, it may also interact with secondary binding sites. On the basis of these findings, molecular modeling studies were intentionally focused on the orthosteric binding cleft to guide the design of new derivatives with improved inhibitory activity.

https://doi.org/10.1021/acsinfecdis.6c00583
ACS Infect. Dis. XXXX, XXX, XXX−XXX

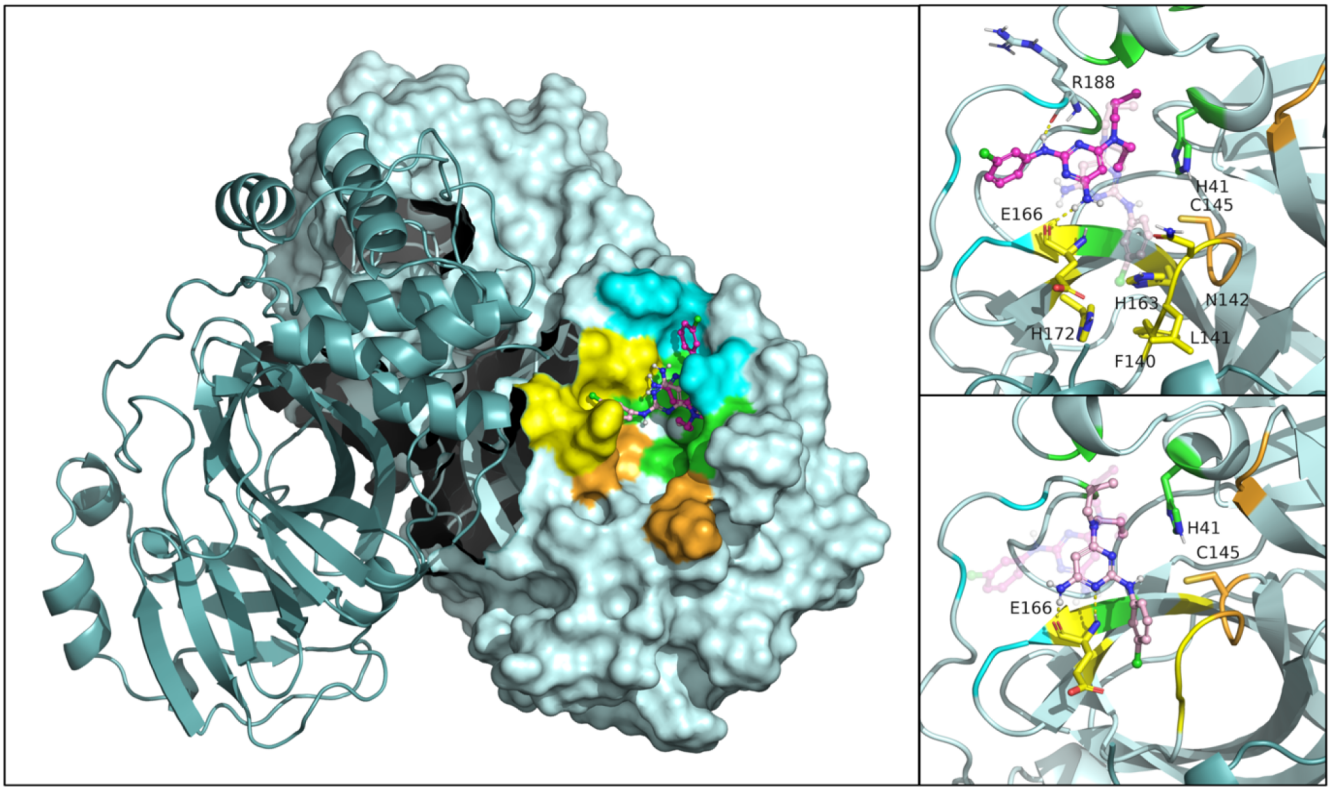

Figure 2. Molecular docking of **4** in SARS-CoV-2 M^{pro} active site. Left: M^{pro} homodimer (protomer A: pale cyan surface; B: deep cyan ribbon) with predicted binding poses. Right: detailed views of the lowest energy pose (magenta, top) and largest cluster pose (pink, bottom). Alternative poses are shown in transparency for comparison. Subsites: *S1* (yellow), *S1′* (orange), *S2* (green), and *S4* (cyan).

Molecular docking[31] of compound **4** revealed two predominant binding modes based on the lowest binding energy and the largest cluster population (Figure 2). In the lowest-energy pose, the C4-amino group was predicted to be oriented toward the amphipathic *S1* subsite,[32] suggesting that modifications at this position could be exploited to optimize interactions within this pocket. Accordingly, a series of derivatives bearing diverse acyl substituents at the 4-amino group (Series **8**) was designed to probe the topological and electronic features of the *S1* region, including the introduction of aromatic groups to enable $\pi-\pi$ stacking with H172 and F140, as well as basic functionalities to establish electrostatic interactions with E166.

In contrast, the most populated docking cluster indicated that the C2-anilino moiety was oriented toward the hydrophobic *S2* subsite. Given the presence of the catalytic residue H41 within this pocket,[32] various groups were introduced to satisfy its lipophilic character and promote favorable stacking interactions with the imidazole ring, thereby enhancing binding stability. Collectively, these docking results suggested that both the *S1* and *S2* subsites could be effectively targeted through systematic modifications of the pyrimidine scaffolds.

Guided by these docking-derived insights, a focused series of pyrimidine derivatives (**5a−d,h,i**, **6a−g**, **7**, **8a−c**, **9d−g**, and **10a,b**; Chart 1) was designed to establish structure−activity relationships (SARs). Structural diversification on the parent scaffold was achieved through systematic modifications, including (i) variation of substituents on the C2-anilino moiety, (ii) incorporation of additional aromatic rings via differently substituted benzyl groups on the C2-anilino moiety to explore the hydrophobic *S2* subsite, (iii) modulation of the C6-amino substituent with saturated heterocycles, and (iv) acylation of the C4-amino group to explore interactions within the *S1* pocket.

In addition, a subset of regioisomers was synthesized to evaluate the impact of positional interchange between the C2-anilino and C6-amino substituents on the biological activity. Lastly, a scaffold hopping strategy was pursued by replacing the pyrimidine core with a pyrimidone one.

Chemistry

The synthesis of compounds **5b−d,h,i**, **6a−e,g**, **7**, **8a−c**, **9d−g**, and **10a,b**, is outlined in Scheme 1 while **4**, **5a**, and **6f** have been synthesized as previously reported.[30]

The 4-amino-2,6-dichloropyrimidine underwent nucleophilic aromatic substitution (S_NAr) with commercially available anilines or [1,1′-biphenyl]-3-amine[33] to afford the 2-anilino regioisomers **11a,h** and **11c,d,i**, via a previously published synthetic strategy.[30,34]

Two alternative green chemistry strategies were explored to perform nucleophilic substitution at C-6 of the pyrimidine core, affording triaminopyrimidines **5b−d,h,i**. In particular, **5b** was prepared by reacting intermediate **11a**[34] with morpholine in water via S_NAr conditions. Alternatively, intermediates **11c,d,i** and **11h** were subjected to microwave-assisted S_NAr with *N,N*-dipropylamine, following an already reported synthetic protocol.[30,34,35]

N-benzylpyrimidines **6b−e,g** were obtained by reacting intermediates **5b−d,h,i** with the corresponding benzyl bromide in the presence of sodium hydride.

An initial attempt to obtain compound **6a** through base-promoted *N*-alkylation of **5a**[30] with 2,4-difluorobenzyl bromide resulted in very low yields (<10%), prompting us to set up an alternative route to obtain this compound. In detail,

https://doi.org/10.1021/acsinfecdis.6c00583
ACS Infect. Dis. XXXX, XXX, XXX−XXX

Scheme 1. Synthetic Route to 5b−d,h,i, 6a−e,g, 7, 8a−c, 9d−g, and 10a,b Compounds[a]

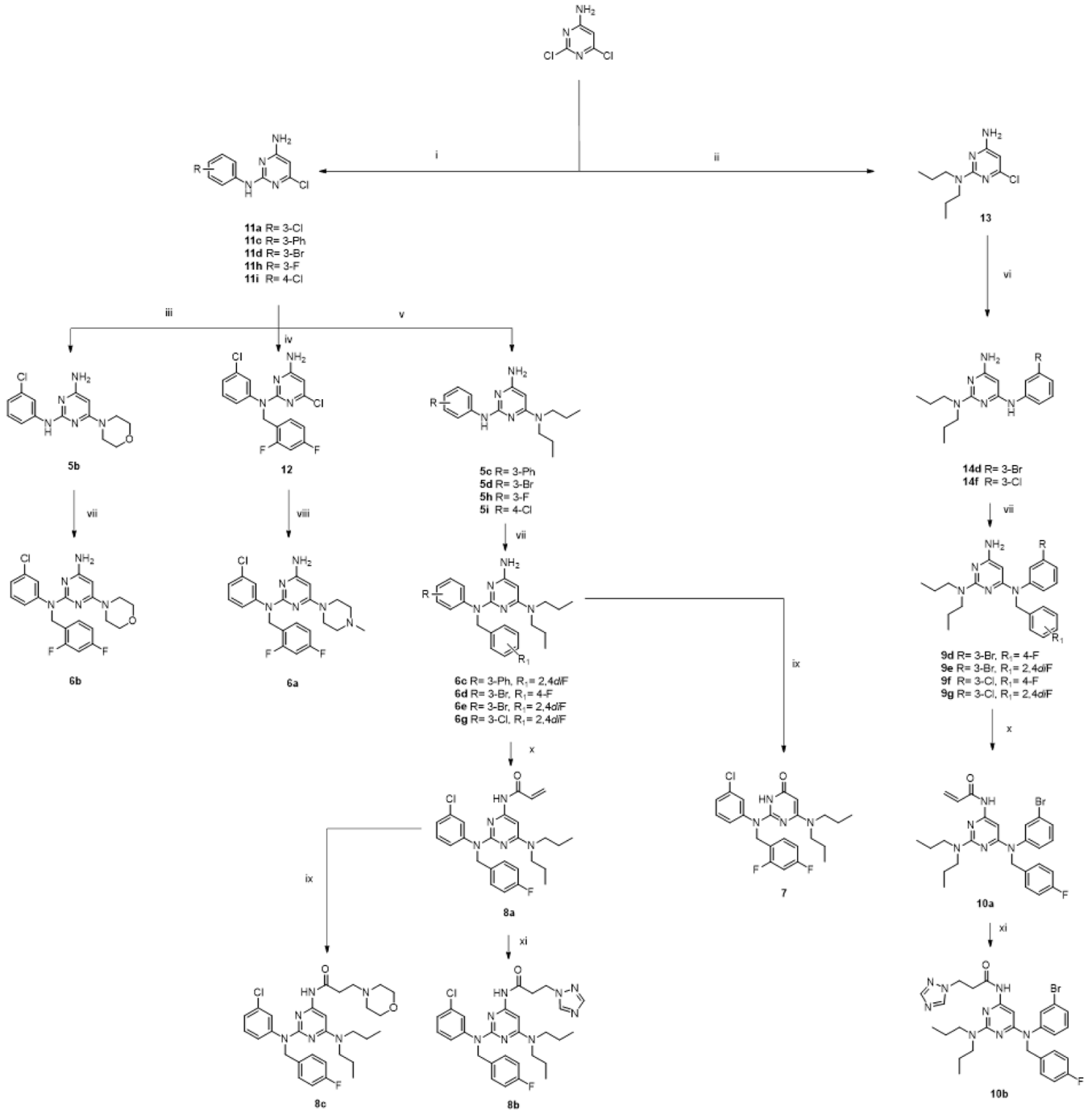

[a]Reagents and conditions: (i) appropriate aniline, 2-methoxyethanol *dry*, reflux, 3−16 h, 40−67% yield; (ii) *N*,*N*-dipropylamine, K_2CO_3 *dry*, DMF *dry*, Ar, 95 °C, 3 h, 64% yield; (iii) morpholine, H_2O, reflux, 3 d, 83% yield; (iv) 2,4-difluorobenzyl bromide, Cs_2CO_3 *dry*, DMF *dry*, rt, 22 h, 37% yield; (v) *N*,*N*-dipropylamine, EtOH, MW, 190 °C, 1.5−2 h, 30−70% yield for **5c,d** or appropriate amine, DIPEA, *i*-PrOH, MW, 180 °C, 2 h, 25−57% yield for **5h,i**; (vi) appropriate aniline, EtOH for compound **14d** or butanol for compound **14f**, HCl 4 N in dioxane, MW, 190 °C, 30 min, 54−95% yield; (vii) proper benzyl bromide, NaH 60%, Ar, DMF *dry*, 0 °C to rt, 2−16 h, 33−80% yield; (viii) *N*-methylpiperazine, EtOH, MW, 190 °C, 30 min, 71% yield; (ix) from **6g**, $NaNO_2$, H_2O/AcOH glacial, rt, 16 h, 60% yield; (x) from **6f** or **9d**, 3-chloropropionyl chloride, Et_3N, DCM, Ar, 0 °C to rt, 16 h, 32−41% yield; (xi) 1,2,4-triazole, Cs_2CO_3 *dry*, AcCN *dry*, Ar, rt for **10b** or 50 °C for **8b**, 16 h, 30−41% yield; morpholine, MeOH, Ar, 0 °C to rt, 16 h, 76% yield for **8c**

intermediate **11a**[34] was first *N*-alkylated with 2,4-difluorobenzyl bromide using cesium carbonate as a base to furnish *N*-benzylpyrimidine **12**, which was subsequently subjected to microwave-assisted S_NAr with 4-methylpiperazine to provide **6a** in a 71% yield.

To obtain pyrimidone **7**, derivative **6g** underwent diazotization and subsequent hydrolysis upon reaction with aqueous sodium nitrite and acetic acid, according to a synthetic protocol already reported by our group.[36]

https://doi.org/10.1021/acsinfecdis.6c00583
ACS Infect. Dis. XXXX, XXX, XXX−XXX

Acrylamide **8a** was obtained by reacting **6f**[30] with 3-chloropropionyl chloride in the presence of triethylamine through nucleophilic acyl substitution and base-promoted *in situ* dehydrochlorination of the 3-chloropropanamide intermediate. The Michael addition of 1,2,4-triazole or morpholine to propenamide **8a** yielded propanamides **8b** and **8c**, respectively.

In order to synthesize the regioisomeric pyrimidines **9d−g**, 4-amino-2,6-dichloropyrimidine underwent an S_NAr reaction with *N,N*-dipropylamine in the presence of potassium carbonate to furnish the 2-regioisomer **13**. This intermediate was then converted into 6-anilino derivatives **14d,f** as hydrochloric salts via HCl-promoted microwave-assisted S_NAr with the appropriate aniline. Subsequent *N*-alkylation with the appropriate benzyl bromide in the presence of sodium hydride afforded the *N*-benzylpyrimidines **9d−g**.

Amides **10a,b** were prepared by the reaction of **9d** with 3-chloropropionyl chloride and triethylamine to give acrylamide **10a**, which was then subjected to Michael addition with 1,2,4-triazole to yield propanamide **10b**.

The detailed synthetic procedures and the analytical and spectroscopic data of the synthesized compounds are reported in the Supporting Information (Experimental Synthesis Procedures and Characterization and Figures S1−S84).

In Vitro Screening for SARS-CoV-2 M^{pro} Inhibition

All compounds were tested *in vitro* in a FRET-based assay against SARS-CoV-2 M^{pro} to evaluate their ability to inhibit the enzymatic activity (Table 1); a concentration of 30 μM was initially selected as a practical screening cutoff. Nirmatrelvir was used as a positive control.

Table 1. Inhibition of SARS-CoV-2 M^{pro} Activity by Hit 4 and Newly Synthesized Compounds

Cpd	SARS-CoV-2 M^{pro} IC_{50} (μM)[a]
4	27.00 ± 3.00
5a	>30
5b	>30
5c	>30
5d	>30
5h	>30
5i	>30
6a	>30
6b	>30
6c	>30
6d	3.00 ± 0.04
6e	>30
6f	>30
6g	24.00 ± 0.76
7	>30
8a	5.15 ± 0.50
8b	17.0 ± 0.68
8c	Fluorescent
9d	1.80 ± 0.50
9e	1.87 ± 0.20
9f	9.27 ± 1.30
9g	9.33 ± 0.10
10a	>30
10b	>30
Nirmatrelvir	0.07 ± 0.02

[a]Concentration reducing SARS-2 M^{pro} activity by 50%. IC_{50} was expressed as means ± SD of three independent experiments.

Among the tested compounds, series **8** and **9** exhibited inhibitory activity against the target, while series **5**, **7**, and **10** showed no detectable activity at the maximum tested concentration. Within series **6**, only two derivatives (**6d** and **6g**) demonstrated enzymatic inhibition.

Preliminary SAR studies indicated that replacing the *N,N*-dipropylamino group of **4** with cyclic aliphatic rings (**5a,b**) or substituting the chlorine atom on the 2-anilino ring with other groups (**5c,d,h,i**) resulted in a complete loss of activity.

Similarly, C2-amino benzylation (series **6**) was generally detrimental, with the exceptions of **6g** (IC_{50} = 24.0 μM) and **6d**, the most active derivative of this series (IC_{50} = 3.00 μM). The scaffold hopping approach to a pyrimidone core (hit **4** vs **7**) also led to a loss of activity.

Conversely, C4-amino acylation of hit **4** (series **8**) led to a modest increase in inhibitory activity, aligning with our computational hypothesis that an acyl group at this position could favor binding. Except for the 3-morpholinopropanoyl compound **8c**, whose activity could not be assessed because of intrinsic fluorescence, both the acryloyl derivative **8a** and the triazolylpropanoyl derivative **8b** showed improved potency compared to the parent hit (IC_{50} = 5.15 and 17.0 μM, respectively). A more favorable trend was observed following the regioisomeric switch between the C2-anilino and C6-amino groups. In particular, the 3-Cl derivatives **9f** and **9g** showed improved potency compared with their corresponding analogues **6f** and **6g** (**9f**: IC_{50}= 9.27 μM; **9g**: IC_{50}= 9.33 μM; **6f**: IC_{50}> 30 μM; **6g**: IC_{50} = 24.0 μM), leading to at least a 2.5-fold increase in activity. A more pronounced effect was observed for the 3-Br analogues **9d** and **9e**, which emerged as the most active within this series, showing a 5-fold increase over their 3-Cl counterparts **9f** and **9g** (**9d**: IC_{50} = 1.80 μM; **9e**: IC_{50} = 1.87 μM).

Conversely, *N*-acylation of series **9** (series **10**) resulted in a loss of activity, indicating that a free amino group is required for activity. Collectively, these findings highlight the importance of the relative positioning of the *N*-benzylanilino and amino substituents in determining inhibitory potency, with the substitution pattern of series **9** being more favorable than that from series **6**. Although the narrow potency range and the presence of several inactive derivatives limit the scope of definitive SAR conclusions, these preliminary data suggest that the pyrimidine core is a suitable scaffold for enzymatic inhibition and that a tentative preference exists for a specific arrangement of the *N*-benzylanilino and amino groups, as observed in series **9**.

Despite being a cysteine protease, SARS-CoV-2 M^{pro} shares structural similarities with the human chymotrypsin serine protease family. Therefore, the selected active compounds were evaluated against human chymotrypsin to assess potential cross-inhibition. None of the tested derivatives showed inhibitory activity up to 30 μM (Table S1), suggesting a favorable selectivity profile of these pyrimidines toward M^{pro}.

SARS-CoV-2 Replication Inhibition

Compounds **6d** and **9d,e** were selected for antiviral assays in SARS-CoV-2-infected cells due to their superior enzymatic inhibition. Additionally, the 3-chlorine derivative **9g** was included to evaluate the impact of potentially higher cellular permeability compared to its 3-bromine counterpart **9e.** The covalent inhibitors nirmatrelvir and GC376 were used as positive controls. Cytotoxicity was first assessed on Vero cells using the RTCA-xCELLigence system. For this purpose, 80% confluent cell monolayers were treated with different concen-

https://doi.org/10.1021/acsinfecdis.6c00583
ACS Infect. Dis. XXXX, XXX, XXX−XXX

Table 2. Antiviral Activity against SARS-CoV-2 and HCoV-229E Replication of Selected Derivatives

	against SARS-CoV-2 replication			against HCoV-229E replication		
Cpd	EC_{50} (μM)[a]	CC_{50} (μM)[b]	SI[c]	72 h EC_{50} (μM)[d]	72 h CC_{50} (μM)[e]	SI[c]
6d	4.96 ± 0.37	85	17.1	1.8 ± 0.28	22.3 ± 8.6	12.4
9d	3.83 ± 0.26	68	17.8	0.87 ± 0.24	38.3 ± 8.3	44.0
9e	4.39 ± 0.37	>100	>22.7	1.66 ± 0.48	18.5 ± 5.1	11.1
9g	9.74 ± 0.85	>100	>10.3	1.72 ± 0.59	17.25 ± 5.8	9.2
Nirmatrelvir	2.42 ± 0.17	>100	>41.3	-	-	-
GC376	2.09 ± 0.08	>100	>47.8	0.24 ± 0.04	>10	>41

[a]Concentration reduced SARS-CoV-2 replication in Vero cells by 50%. [b]Concentration reduced Vero cell viability by 50%. [c]SI = CC_{50}/EC_{50}. [d]Concentration reduced HCoV-229E replication in Beas2B cells by 50%. [e]Concentration reducing Beas2B cell viability by 50%. Values are expressed as means ± SD from three independent experiments, in triplicate.

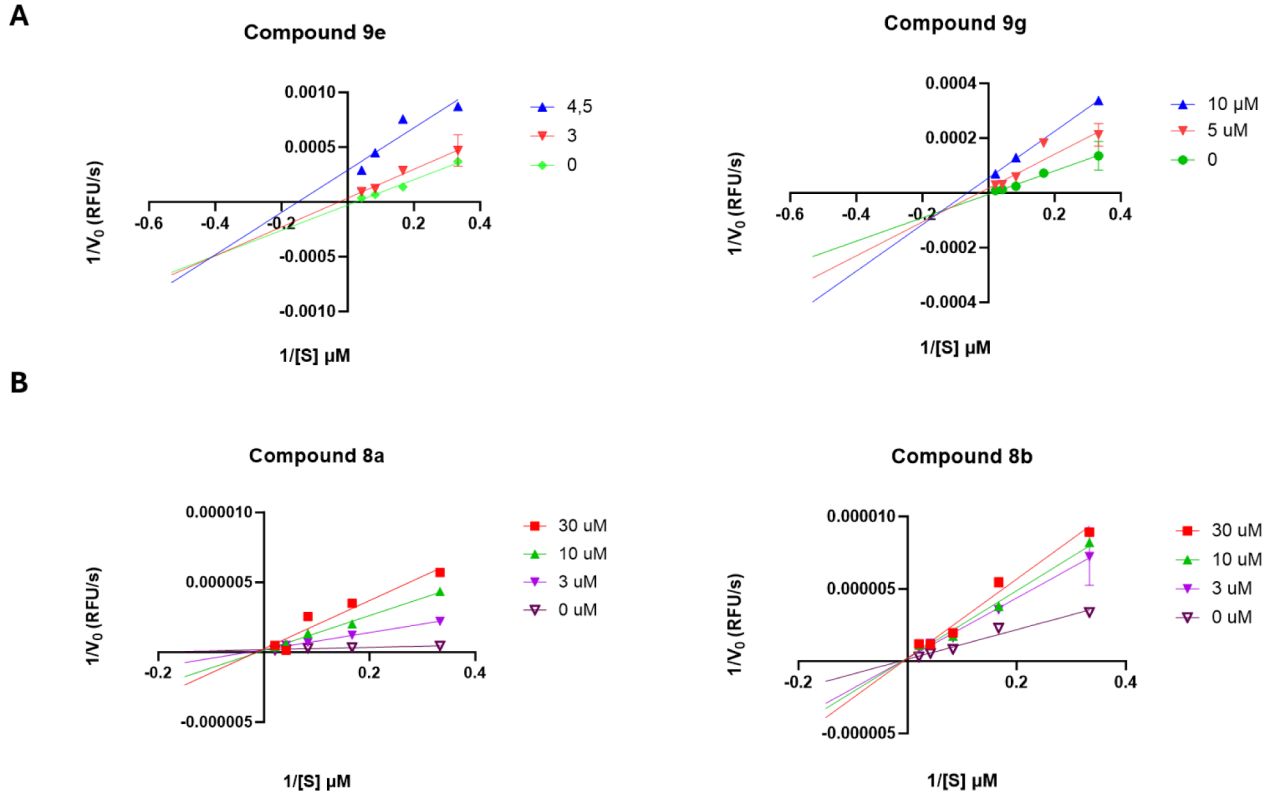

Figure 3. Lineweaver–Burk plots of **9e–9g** (Panel A) and **8a–8b** (Panel B) against SARS-CoV-2 M^{pro}. Reciprocal reaction velocity (RFU/s) was plotted against the reciprocals of the substrate (μM) in the presence of varying both inhibitor and substrate concentrations.

trations (100–50–25 μM) of compounds. The real-time changes in cell index were monitored every 5 min, and at 24 h, the half-maximal cytotoxic concentration (CC_{50}) was calculated. **6d** and **9d** showed a CC_{50} of 85 μM and 68 μM, respectively, whereas **9e** and **9g** showed no cytotoxic effect. Based on these results, the antiviral activity of the derivatives was tested in the range from 0.78 μM to 50 μM through plaque assay. The antiviral activity was assessed by the calculation of the 50% inhibitory concentration (EC_{50}) from the experimental curves (Supporting Information, Figure S86).

As summarized in Table 2, all compounds inhibit SARS-CoV-2 viral replication with EC_{50} values lower than 10 μM. The highest potencies were observed for **6d** (EC_{50} = 4.96 μM), **9e** (EC_{50} = 4.39 μM), and **9d** (EC_{50} = 3.82 μM), whereas **9g** exhibited a slight reduction in inhibitory potency with an EC_{50} of 9.74 μM. The 95% confidence interval (CI) for each compound was: **6d**: 4.121–5.991; **9d**: 3.348–4.365; **9e**: 3.719–5.184; **9g**: 8.209–11.57. Based on these results, the derivative **9e** resulted as the best and most promising among all the tested triaminopyrimidines, also exhibiting the higher selectivity index (SI).

Broad Spectrum Activity of 6d and 9d,e,g

Compounds active against SARS-CoV-2 viral replication, **6d and 9d,e,g**, were further evaluated against human alphacoronavirus 229E (HCoV-229E) in order to assess their potential broad-spectrum antiviral activity. Compound **9d** exhibited the most potent antiviral effect with an EC_{50} value of 0.87 (Table 2) with only moderate cytotoxicity, resulting in a promising SI of 44. On the other hand, compounds **6d**, **9e**, and **9g** showed comparable antiviral activity but lower selectivity indices. Overall, these results demonstrate that pyrimidine scaffold optimization led to derivatives with significant anti-SARS-CoV-2 and HCoV-229E activity, with **9d** showing the most favorable profile.

https://doi.org/10.1021/acsinfecdis.6c00583
ACS Infect. Dis. XXXX, XXX, XXX–XXX

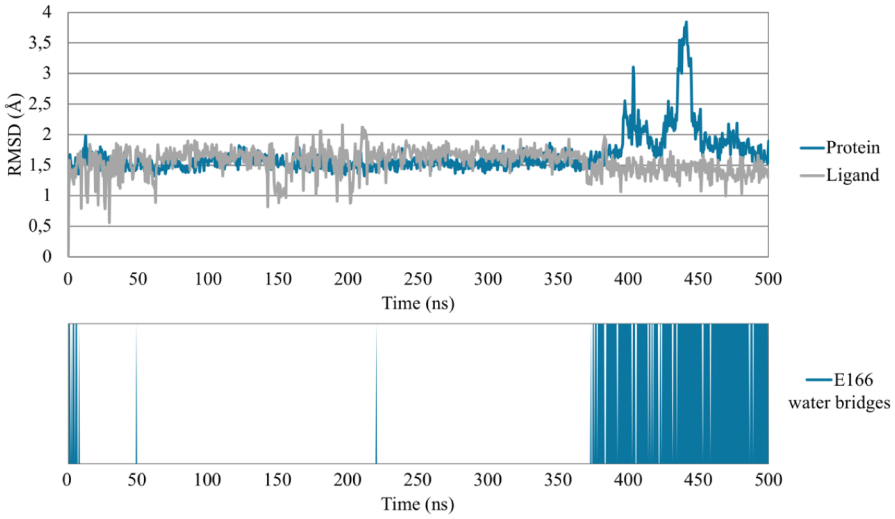

Figure 4. Structural stability and interaction profile of MD simulation performed on **9d**-M^{pro} complex. Upper panel: RMSD profiles for protein backbone (blue) and ligand (gray). Lower panel: timeline representation highlighting the occurrence of water-mediated bridges between ligand and E166.

Mechanism of Action on SARS-CoV-2 M^{pro} Activity

To further elucidate the mechanism of action (MoA) of this new chemotype of Mpro inhibitors, compounds **9e**, **9g**, **8a**, and **8b** were selected for in-depth kinetic studies. Compounds **9e** and **9g** were chosen as they exhibited the most potent inhibition in both enzymatic and cellular assays, while **8a** and **8b** were examined to assess whether the introduction of bulkier substituents on the pyrimidine scaffold could affect the kinetics of inhibition.

The inhibition kinetics were evaluated by varying both substrate and inhibitor concentrations, and the resulting data were analyzed using Lineweaver−Burk plots (Figure 3).

Michaelis−Menten analysis revealed that **9e** and **9g** displayed a mixed mode of inhibition, resulting in a decrease in both apparent V_{max} and K_M based on the Michaelis−Menten equation (data not shown). The mixed model of inhibition is confirmed by the Lineweaver−Burk plot, where lines intersect below the negative half of the *X*-axis (Panel A), indicating a change in apparent enzyme−substrate affinity without direct competition with the substrate.

Compounds **8a** and **8b** did not affect the V_{max} but caused a concentration-dependent increase of the K_M (panel B), indicating a reduction in enzyme affinity for the substrate and suggesting a competitive MoA, as confirmed by the intersection of lines on the *Y*-axis of the Lineweaver−Burk plot.

The distinct kinetic profiles observed for the two series suggest different modes of interaction with the SARS-CoV-2 M^{pro}. While compounds **8a** and **8b** behave as classical competitive inhibitors, likely interfering directly with substrate binding at the active site, compounds **9e** and **9g** display a mixed-type inhibition, indicating that their inhibitory activities cannot be explained solely by substrate competition. In mixed inhibition, the observed decrease in both V_{max} and K_M can be attributed to the binding of the inhibitors to both free enzyme and the enzyme−substrate complex and is consistent with ligand-induced conformational changes that affect both substrate binding and catalytic efficiency.

These findings suggest that structural differences in the substituents of the pyrimidine scaffold may influence the binding mode within the active site, causing a different impact on the M^{pro} recognition of the peptide substrate.

Molecular Modeling

To elucidate M^{pro} fundamental inhibition requirements, molecular modeling studies were focused on the orthosteric active site targeted by all of these derivatives regardless of whether they exhibited purely competitive (**8a,b**) or mixed-type (**9e,g**) inhibition kinetics. Simulations were performed on structurally representative compounds: **6d** and **9d** were selected as representative C2-benzyl-substituted regioisomers, while **8b** was included as a representative member of the acylated series.

Figure S87 (Supporting Information) illustrates the binding poses for **6d** and **8b**. During ligand preparation, pK_a calculations were performed to assess the protonation state of N^1. For **6d**, the pK_a of 7.4 suggested a 50% protonation state at physiological pH, meaning that both neutral and protonated species are expected to coexist at physiological pH, but for both forms, the binding mode closely mirrors the one proposed for the hit **4** (Figure 2). The pyrimidine core adopted an orientation compatible with the formation of key hydrogen bonds with the E166 backbone (N^3 acts as an H-bond acceptor, and aniline NH_2 is properly oriented to act as a donor). Additionally, the deprotonated form engages in $\pi-\pi$ stacking with H41, which may also act as a H-bond donor toward the halogen atom. The protonated state facilitates a cation−π interaction with the same residue. In contrast, the pyrimidine core of **8b** deviates from the binding orientations of **4** and **6d**. As hypothesized, the acylated moiety occupies the *S1* subsite, where the triazole ring accepts H-bonds from the N142 side chain and backbone, while its aryl substituents project toward the hydrophobic *S4* subsite.

The binding mode of **9d** was investigated using the same docking protocol, and then its binding pose was validated via MD simulations. Analysis of the trajectories (Figure 4) showed high ligand stability with a mean Root-Mean-Square Deviation (RMSD) of 1.56 Å (range: 0.56−2.16 Å), confirming that **9d** remains firmly anchored within the pocket without undergoing drastic conformational changes or detachment events. While the ligand reached equilibrium quickly, the protein underwent a transient structural rearrangement (RMSD peaking at ∼4.0 Å) before stabilizing between 1.5 and 1.8 Å after 450 ns.

https://doi.org/10.1021/acsinfecdis.6c00583
ACS Infect. Dis. XXXX, XXX, XXX−XXX

Trajectory visual inspection highlighted the pivotal role of residue E166 during the final 150 ns. This residue forms stable water-mediated interactions with the aniline NH_2 group and the N^3 atom. As shown in Figures 4 and 5, the frequency of these

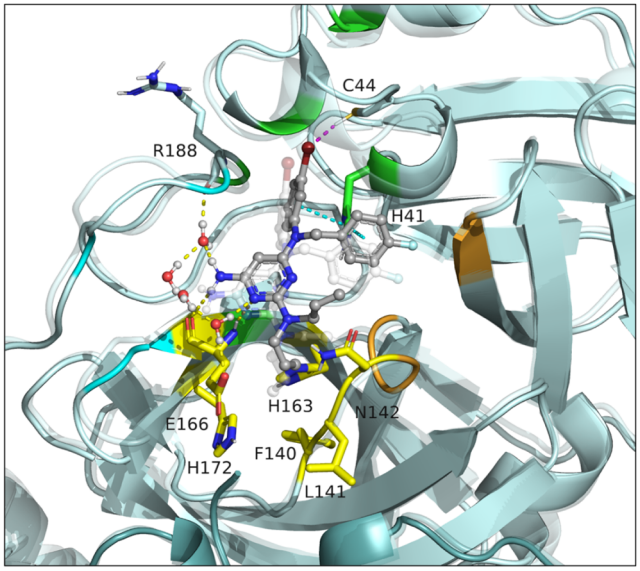

Figure 5. Representative binding mode of **9d** (gray sticks). The pose was identified via ligand clustering analysis performed on the final 150 ns of the MD simulation trajectory. The initial complex (derived from molecular docking) is shown in transparency. Subsite residues are color-coded according to Figure 2.

water bridges increases significantly in the late stages of the simulation, persisting even after the protein returns to a stable conformation (RMSD < 2 Å).

Figure 5 illustrates the representative pose of **9d** from ligand clustering performed on the last 150 ns of simulation. Beyond the previously discussed water bridges mediated by the main and side chains of E166 (which may also involve the backbones of neighboring residues), the catalytic H41 is engaged in $\pi-\pi$ stacking with both N^6-aryl rings, while the bromine atom is favorably oriented to establish a H-bond with C44.

In this context, it is noteworthy that E166 plays a pivotal role in the binding of **9d**. E166 acts as a critical structural pivot for M^{pro}.[37−39] Located at the heart of the dimer interface, its carboxylic side chain serves as a hydrogen bond acceptor for the N-terminal ammonium group and the side chain hydroxyl of S1 from the adjacent protomer. This interaction anchors the "N-finger" of the partner protomer in the proper orientation, a prerequisite for maintaining the catalytically competent dimeric conformation. Additionally, E166 maintains the *S1* pocket rigidity through an intramolecular H-bond network with H172.

Notably, comparison of the predicted binding poses of **6d**, **8b**, and **9d** (Figures 5 and S87) further supports the central role of E166 during the binding of this new class of inhibitors. In detail, compound **6d** maintains the pyrimidine core orientation observed for **9d**, whereas the triazole ring of **8b** occupies the E166-associated *S1* subsite. These shared interaction patterns suggest that the E166-mediated stabilization observed for **9d** may also contribute to the binding of **6d** and **8b**. To directly evaluate the contribution of this residue to ligand binding, site-directed mutagenesis experiments were conducted.

Evaluation of Compounds on SARS-CoV-2 M^{pro} E166V Mutant

To experimentally validate the mechanistic role of E166 suggested by docking and MD hypotheses, mutagenesis studies were conducted to generate the SARS-CoV-2 M^{pro} E166V variant. The E166V mutation is a substitution known to confer resistance to inhibitors like nirmatrelvir by disrupting key interactions within the S1 binding pocket.[39] A decreased sensitivity was also observed for ensitrelvir, ibuzatrelvir, and related noncovalent M^{pro}-targeting agents.[40]

In contrast, no effect was observed on GC376 due to its ability to avoid unfavorable contacts with V166 through conformational flexibility, which allows two different conformations, both of which point away from this residue.[41]

Based on literature data[37−39] and modeling results, we hypothesize that E166 contributes to inhibitor recognition through two complementary mechanisms. First, substitution of glutamate with valine abolishes the direct hydrogen-bonding and water-mediated interaction network observed for **9d** and predicted for **6d**. Second, the introduction of the β-branched valine side chain perturbs the geometry of the *S1* subsite, compromising the accommodation of ligands that rely on this pocket, particularly acylated derivatives such as **8b**. Consistent with these predictions, biological evaluation of the E166V mutant (Table S2) revealed a complete loss of inhibitory activity for **6d**, **8b**, and **9d**.

To assess whether this dependence is common across the chemotype, the analysis was expanded to include the acylated analogue **8a** and the regioisomeric series **9e−g**. Given their close structural relationship to **9d**, these compounds were expected to engage a similar E166-centered interaction network. Indeed, all analogues exhibited a marked loss of activity against the E166V variant (Table S2) and given the well-established role of E166 in maintaining the active-site architecture, these data confirm that this class of inhibitors strictly relies on interactions within the orthosteric pocket for their inhibitory effect.

These findings align with the computational studies presented, highlighting the indispensable role of E166 in both the binding and potency of this chemical series. Nirmatrelvir, used as a positive control, also exhibited a >100-fold loss of potency against the E166V mutant, underscoring that its efficacy is strictly dependent on structural integrity and specific interactions within the *S1* subsite.[38]

CONCLUSIONS

In this study, we report the rational optimization of a 2,4,6-triaminopyrimidine scaffold, leading to the identification of low-micromolar SARS-CoV-2 M^{pro} inhibitors. SARs demonstrated that regioisomeric switching combined with strategic benzyl substitution markedly enhances the *in vitro* potency of the compounds against recombinant SARS-CoV-2 M^{pro}, with **9d** and **9e** emerging as the most active derivatives. Importantly, these compounds translate enzymatic inhibition into effective viral replication suppression not only in SARS-CoV-2 but also in HCoV-229E cells, suggesting that this scaffold may be useful to develop broad-spectrum coronavirus inhibitors.

Mechanistic investigations revealed that subtle structural modifications dictate distinct inhibition modalities ranging from competitive to mixed mechanisms. Computational modeling and mutagenesis experiments consistently identified residue E166 as a critical determinant for ligand binding and pocket integrity.

https://doi.org/10.1021/acsinfecdis.6c00583
ACS Infect. Dis. XXXX, XXX, XXX−XXX

Collectively, our findings validate the pyrimidine core as a versatile platform for M^{pro} targeting and establish clear structural and mechanistic guidelines for the design of next-generation antiviral agents with improved potency and resistance profiles.

MATERIALS AND METHODS

Chemistry

Chemical, physical, analytical, and spectroscopic data for derivatives **5b−d,h,i**, **6a−e,g**, **7**, **8a−c**, **9d−g**, 10a,b, 11c,d,i, **12, 13**, and **14d,f** are reported in the Supporting Information (Experimental Synthesis Procedures and Characterization and Figures S1−S84). Syntheses and characterization of **4, 5a, 6f**, and **11a,h** are described in the literature.[30,34]

Biological Assays

Data Analysis. Data analysis of assay development results was performed using GraphPad Prism Version 9.1.2. Test compound results were normalized relative to respective controls. Dose-response curves were fitted to a nonlinear regression of ($\log_{10}$) dose vs normalized response-variable slope. Assay quality was assessed using the Z′-factor calculation with $Z' > 0.5$ as the acceptance threshold.

Virus Production

A virus working stock was prepared by propagating a strain of SARS-CoV-2, variant omicron XBB.1.16.11 (hCoV-19/Italy/LAZ-DIBS-230829301/2023), isolated from a nasopharyngeal swab by the Defense Institute for Biomedical Sciences, Rome, Italy, in Vero E6 cells cultured in minimum essential medium (MEM) containing 2% (w/v) fetal bovine serum (Euroclone S.p.A.). 72 h after the infection, supernatants containing the released viral particles were collected and clarified by centrifugation at 600 *g* for 5 min. Virus stocks were kept at −80 °C until use, and the viral titer was determined by plaque assay. The swab was accompanied by signed informed consent.

SARS-CoV-2 Plaque Assay

Vero E6 cells (Sigma-Aldrich) were seeded into 24-well plates until confluency and then infected for 1 h at 37 °C with SARS-CoV-2 using a 0.01 multiplicity of infection (MOI). After 1 h of incubation, the inoculum was replaced with fresh medium supplemented with 2% FBS and containing each derivative at varying concentrations. Untreated infected cells were used as positive controls. After 24 h, the supernatants were collected, and a plaque assay was performed. Briefly, the collected supernatants were used to infect Vero E6 cells seeded in a 12-well plate for 1 h at 37 °C. Then, the inoculum was removed, and the medium was replaced with a mixture of MEM (no glutamine, no phenol red, Gibco-Thermo Fisher Scientific S.p.A.), containing Non-Essential Amino Acid Solution (NEAA) 1× (Gibco), 1.5% Tragacanth (Sigma-Aldrich-Merck), $NaHCO_3$ 7% (Gibco), l-glutamine 1× (Gibco), 0.02 M Hepes (Euroclone S.p.A.), Dimethyl Sulfoxide (DMSO) (Sigma-Aldrich-Merck), and 2% FBS (Gibco). Three days postinfection, the mixture was carefully removed, plates were washed with saline solution, stained with 1% crystal violet for 10 min, and plaque-forming units (PFU) were counted. The plaque reduction ratio was calculated as $(100 - N/N_0 \times 100)$, where N is the PFU count of the treated sample, and N_0 is the PFU count of the control sample. The plaque assay was also used to determine the concentration of molecules that inhibits 50% of the viral titer in each well (IC_{50}). Compounds have been tested at concentrations ranging from 0.78 to 50 μM. Untreated infected cells were used as a positive control of viral infection (2×10^3 PFU/mL) and the EC_{50} was calculated.

Cellular Toxicity Assay

Cytotoxicity assay was performed using the label-free real-time cell analysis RTCA-xCELLigence (Agilent Technologies).[42] Vero E6 cells were plated at a final density of 2×10^4 per well within the real-time cell analyzer unit for culture. After 24 h, at the plateau phase of the growth cell curve, scalar concentrations of compounds (from 100 μM to 25 μM) were introduced in triplicate. Impedance signals were recorded at 5 min intervals for 24 h, and then the CC_{50} was calculated through the RTCA software Pro (Version 2.9.0), using the sigmoidal dose−response curve with a variable slope.

HCoV-229E Assay

The evaluation of compounds against hCoV-229E replication was performed as previously described.[43]

Transformation and Expression

A pET-28b plasmid (200 ng) containing the recombinant gene of the SARS-CoV-2 M^{pro} protein (MN975262) was used to transform *E. coli* BL21(DE3) strain, and the protein was expressed as previously described.[13]

Purification

The bacterial pellet was purified using the protocol described in Stefanelli et al. 2023[13] with an additional step. Briefly, the eluted M^{pro} was collected and purified by size exclusion chromatography (SEC) using a Superdex 16/600 column (Cytiva), equilibrated with a buffer containing 20 mM Tris-HCl pH 7.8, 1 mM DTT. The peak fractions were collected, and the protein purity was assessed by SDS-PAGE.

SARS-CoV-2 Assay

M^{pro} enzymatic activity was evaluated using a FRET-based assay in a 384-well format. The recombinant M^{pro} was incubated at a concentration of 50 nM for 30 min at 37 °C in a reaction mix containing 20 mM Tris-HCl pH 7.3, 100 mM NaCl, 0.005 mM TCEP, 0.10% BSA, and 1 mM EDTA. The enzymatic reaction was initiated by the addition of 12 μM DABCYL-KTSAVLQ↓SGFRKM-EDANS substrate (DBA Italia), and the fluorescence signal was recorded for 15 min using Victor Nivo (PerkinElmer) at 320/480 nm.[44]

The same protocol was used for the kinetics of inhibition of the selected compounds, except for compound and substrate concentration. Results were plotted in a Lineweaver−Burk graph as reciprocals of reaction velocity (RFU/sec) against the reciprocals of substrate (μM) in the presence of different inhibitor concentrations using the software GraphPad Prism 9.

Chymotrypsin Assay

Selectivity was evaluated using a chymotrypsin activity assay kit (abx298848, Abbexa) according to manufacturer's instructions. Compounds were tested at a concentration of 30 μM, and the negative control was DMSO at 0.5%. Cleaved substrate was detected at Ex/Em = 380/460 nm.[45]

Molecular Modeling

The M^{pro} crystal structure (PDB: 8DZ2)[46] was refined using the Maestro Protein Preparation Wizard,[47] including hydrogen addition, solvent removal, and protonation/tautomeric states at physiological pH. Ligands were modeled and minimized *via* LigPrep (OPLS4 force field, pH = 7.4 ± 0.00). pK_a calculations (Jaguar[47]) revealed **8b** and **9d** as neutral (protonation fraction <10%), while **6d** ($pK_a \simeq 7.4$) was considered in both neutral and protonated states.

Docking simulations were performed using AD4-GPU.[31] Receptors and ligands were converted to PDBQT format using AutoDockTools (Gasteiger charges/torsional parameters). A 20 × 20 × 20 Å grid box (spacing: 0.375 Å) was centered on the cocrystallized ligand binding site. For each compound, 100 Lamarckian Genetic Algorithm (LGA) runs were executed; poses were clustered (2.0 Å RMSD cutoff) and ranked by ΔG_{AD4}.

9d-M^{pro} complex was simulated using Desmond[47] in an orthorhombic TIP3P water box (10 Å buffer, 0.15 M NaCl). Following multistage equilibration under the OPLS4 force field, a 500 ns production run (NPT ensemble, 300 K, 1 bar) was performed. Trajectories were analyzed *via* the Desmond SID tool.[47] Representative binding poses were identified through ligand clustering (2.0 Å RMSD cutoff) over the final 150 ns of the trajectory using the Desmond clustering panel.[47]

Visualizations were rendered using PyMOL.[48]

Mutagenesis

Amino acid substitutions were introduced into the pET-28b plasmid of the SARS-CoV-2 M^{pro} sequence using a QuikChange mutagenesis kit

https://doi.org/10.1021/acsinfecdis.6c00583
ACS Infect. Dis. XXXX, XXX, XXX−XXX

(Agilent Technologies Inc.) following the manufacturer's instructions. The obtained plasmids were used for the expression and the purification of SARS-CoV-2 M^{pro} mutants using the protocol described in Materials and Methods.

■ ASSOCIATED CONTENT

Supporting Information

The Supporting Information is available free of charge at https://pubs.acs.org/doi/10.1021/acsinfecdis.6c00583.

General and specific procedures for all the derivatives (Pages S3−S16); FTIR, ^{1}H NMR, and ^{13}C NMR spectra of final compounds (Figures S1−S84); dose−response curves of compounds **4**, **6d**,**g**, **8a**,**b**, **9d**−**g**, and nirmatrelvir inhibiting SARS-CoV-2 M^{pro} activity (Figure S85); the antiviral effect of **6d**, **9g**, **9e**, **9d,** nirmatrelvir, and GC376 against SARS-CoV-2 (Figure S86); evaluation of selected compounds' activity against chymotrypsin (Table S1); predicted binding poses for **6d** and **8b** (Figure S87); the effect of selected compounds on SARS-CoV-2 M^{pro} wt and E166V mutant activities (Table S2) (PDF)

■ AUTHOR INFORMATION

Corresponding Author

Roberta Costi − *Department of Chemistry and Pharmaceutical Technologies, Istituto Pasteur-Fondazione Cenci Bolognetti, "Sapienza" Università di Roma, Rome I-00185, Italy;* orcid.org/0000-0002-1314-9029; Phone: +39 0649693247; Email: roberta.costi@uniroma1.it

Authors

Salvatore Nieddu − *Department of Life and Environmental Sciences, Cittadella Universitaria di Monserrato, University of Cagliari, Cagliari, Monserrato SS-554, Italy*

Giuseppe Ruggieri − *Department of Chemistry and Pharmaceutical Technologies, Istituto Pasteur-Fondazione Cenci Bolognetti, "Sapienza" Università di Roma, Rome I-00185, Italy; Department of Public Health, Experimental Medicine and Forensic, University of Pavia, Pavia 27100, Italy;* orcid.org/0009-0004-3911-6833

Riccardo De Santis − *Defence Institute for Biomedical Sciences, Rome 00184, Italy; Department of Public Health and Infectious Diseases, "Sapienza" Università di Roma, Rome 00185, Italy*

Paolo Malune − *Department of Life and Environmental Sciences, Cittadella Universitaria di Monserrato, University of Cagliari, Cagliari, Monserrato SS-554, Italy*

Elisa Patacchini − *Department of Chemistry and Pharmaceutical Technologies, Istituto Pasteur-Fondazione Cenci Bolognetti, "Sapienza" Università di Roma, Rome I-00185, Italy;* orcid.org/0000-0002-4531-3612

Valentina Noemi Madia − *Department of Science, Roma Tre University, Rome 00146, Italy;* orcid.org/0000-0002-5724-612X

Francesco Saccoliti − *Department of Life Science, Health, and Health Professions, Link Campus University, Rome I-00165, Italy;* orcid.org/0000-0002-2907-5503

Antonella Messore − *Department of Life Science, Health, and Health Professions, Link Campus University, Rome I-00165, Italy;* orcid.org/0000-0003-0158-5816

Laura Zarbo − *Department of Chemistry and Pharmaceutical Technologies, Istituto Pasteur-Fondazione Cenci Bolognetti, "Sapienza" Università di Roma, Rome I-00185, Italy;* orcid.org/0009-0009-3724-4133

Angela Corona − *Department of Life and Environmental Sciences, Cittadella Universitaria di Monserrato, University of Cagliari, Cagliari, Monserrato SS-554, Italy;* orcid.org/0000-0002-6630-8636

Donatella Amatore − *Defence Institute for Biomedical Sciences, Rome 00184, Italy*

Giorgia Grilli − *Defence Institute for Biomedical Sciences, Rome 00184, Italy*

Alessandra Amoroso − *Defence Institute for Biomedical Sciences, Rome 00184, Italy*

Florigio Lista − *Defence Institute for Biomedical Sciences, Rome 00184, Italy*

Enzo Tramontano − *Department of Life and Environmental Sciences, Cittadella Universitaria di Monserrato, University of Cagliari, Cagliari, Monserrato SS-554, Italy*

Roberto Di Santo − *Department of Chemistry and Pharmaceutical Technologies, Istituto Pasteur-Fondazione Cenci Bolognetti, "Sapienza" Università di Roma, Rome I-00185, Italy;* orcid.org/0000-0002-4279-7666

Francesca Esposito − *Department of Life and Environmental Sciences, Cittadella Universitaria di Monserrato, University of Cagliari, Cagliari, Monserrato SS-554, Italy;* orcid.org/0000-0001-9725-7977

Complete contact information is available at: https://pubs.acs.org/10.1021/acsinfecdis.6c00583

Author Contributions

◆S.N., G.R., R.D. Santis, R.D. Santo, and F.E. contribute equally. The manuscript was written through contributions of all authors. All authors have given approval to the final version of the manuscript.

Funding

This work was supported by EU funding within the Next Generation EU-MUR PNRR Extended Partnership initiative on Emerging Infectious Diseases (PE00000007, INF-ACT, Spoke 5), Next Generation EU-MUR PRIN 2022 project code 20228NPP2Y, and Ateneo 2024 (project code RG124190BB0EB5C9).

Notes

The authors declare no competing financial interest.

■ REFERENCES

(1) V'kovski, P.; Kratzel, A.; Steiner, S.; Stalder, H.; Thiel, V. Coronavirus biology and replication: implications for SARS-CoV-2. *Nat. Rev. Microbiol.* **2021**, *19* (3), 155−170.

(2) Otter, J. A.; Donskey, C.; Yezli, S.; Douthwaite, S.; Goldenberg, S. D.; Weber, D. J. Transmission of SARS and MERS coronaviruses and influenza virus in healthcare settings: the possible role of dry surface contamination. *J. Hosp. Infect.* **2016**, *92* (3), 235−250.

(3) Lu, R.; Zhao, X.; Li, J.; Niu, P.; Yang, B.; Wu, H.; Wang, W.; Song, H.; Huang, B.; Zhu, N.; Bi, Y.; Ma, X.; Zhan, F.; Wang, L.; Hu, T.; Zhou, H.; Hu, Z.; Zhou, W.; Zhao, L.; Chen, J.; Meng, Y.; Wang, J.; Lin, Y.; Yuan, J.; Xie, Z.; Ma, J.; Liu, W. J.; Wang, D.; Xu, W.; Holmes, E. C.; Gao, G. F.; Wu, G.; Chen, W.; Shi, W.; Tan, W. Genomic characterisation and epidemiology of 2019 novel coronavirus: implications for virus origins and receptor binding. *Lancet* **2020**, *395* (10224), 565−574.

(4) Yang, H.; Rao, Z. Structural biology of SARS-CoV-2 and implications for therapeutic development. *Nat. Rev. Microbiol.* **2021**, *19* (11), 685−700.

(5) Tam, D.; Lorenzo-Leal, A. C.; Hernández, L. R.; Bach, H. Targeting SARS-CoV-2 Non-Structural Proteins. *Int. J. Mol. Sci.* **2023**, *24* (16), 13002.
(6) Hu, Q.; Xiong, Y.; Zhu, G. H.; Zhang, Y. N.; Zhang, Y. W.; Huang, P.; Ge, B. X. The SARS-CoV-2 main protease (Mpro): Structure, function, and emerging therapies for COVID-19. *MedComm* **2022**, *3* (3), No. e151.
(7) Gorkhali, R.; Koirala, P.; Rijal, S.; Mainali, A.; Baral, A.; Bhattarai, H. K. Structure and Function of Major SARS-CoV-2 and SARS-CoV Proteins. *Bioinforma. Biol. Insights* **2021**, *15*, 11779322211025876.
(8) Parmar, M.; Thumar, R.; Patel, B.; Athar, M.; Jha, P. C.; Patel, D. Structural differences in 3C-like protease (Mpro) from SARS-CoV and SARS-CoV-2: molecular insights revealed by Molecular Dynamics Simulations. *Struct. Chem.* **2022**, 1−18.
(9) Zian, D.; Iaconis, D.; Nenci, S.; Crusco, A.; Tawde, S.; Sodano, M.; Vitalone, R.; Raje, A.; Palamini, M.; Carettoni, D.; Molteni, A.; Manelfi, C.; Tazzari, V.; Beccari, A. R.; Malune, P.; Maloccu, S.; Paulis, A.; Corona, A.; Nieddu, S.; Coletti, S.; Scarabottolo, L.; Tramontano, E.; Esposito, F.; Catalani, M. The efficiency of high-throughput screening (HTS) and in-silico data analysis during medical emergencies: Identification of effective antiviral 3CLpro inhibitors. *Antiviral Res.* **2025**, *237*, 106119.
(10) Messore, A.; Malune, P.; Patacchini, E.; Madia, V. N.; Ialongo, D.; Arpacioglu, M.; Albano, A.; Ruggieri, G.; Saccoliti, F.; Scipione, L.; Tramontano, E.; Canton, S.; Corona, A.; Scognamiglio, S.; Paulis, A.; Suleiman, M.; Al-Maqtari, H. M.; Abid, F. M. A.; Kawsar, S. M. A.; Sankaranarayanan, M.; Di Santo, R.; Esposito, F.; Costi, R. New Thiazolidine-4-One Derivatives as SARS-CoV-2 Main Protease Inhibitors. *Pharmaceuticals* **2024**, *17* (5), 650.
(11) Vuong, W.; Fischer, C.; Khan, M. B.; van Belkum, M. J.; Lamer, T.; Willoughby, K. D.; Lu, J.; Arutyunova, E.; Joyce, M. A.; Saffran, H. A.; Shields, J. A.; Young, H. S.; Nieman, J. A.; Tyrrell, D. L.; Lemieux, M. J.; Vederas, J. C. Improved SARS-CoV-2 Mpro inhibitors based on feline antiviral drug GC376: Structural enhancements, increased solubility, and micellar studies. *Eur. J. Med. Chem.* **2021**, *222*, 113584.
(12) Ambrosio, F. A.; Costa, G.; Romeo, I.; Esposito, F.; Alkhatib, M.; Salpini, R.; Svicher, V.; Corona, A.; Malune, P.; Tramontano, E.; Ceccherini-Silberstein, F.; Alcaro, S.; Artese, A. Targeting SARS-CoV-2 Main Protease: A Successful Story Guided by an In Silico Drug Repurposing Approach. *J. Chem. Inf. Model.* **2023**, *63* (11), 3601−3613.
(13) Stefanelli, I.; Corona, A.; Cerchia, C.; Cassese, E.; Improta, S.; Costanzi, E.; Pelliccia, S.; Morasso, S.; Esposito, F.; Paulis, A.; Scognamiglio, S.; Di Leva, F. S.; Storici, P.; Brindisi, M.; Tramontano, E.; Cannalire, R.; Summa, V. Broad-spectrum coronavirus 3C-like protease peptidomimetic inhibitors effectively block SARS-CoV-2 replication in cells: Design, synthesis, biological evaluation, and X-ray structure determination. *Eur. J. Med. Chem.* **2023**, *253*, 115311.
(14) Owen, D. R.; Allerton, C. M. N.; Anderson, A. S.; Aschenbrenner, L.; Avery, M.; Berritt, S.; Boras, B.; Cardin, R. D.; Carlo, A.; Coffman, K. J.; et al. An oral SARS-CoV-2 Mpro inhibitor clinical candidate for the treatment of COVID-19. *Science* **2021**, *374* (6575), 1586−1593.
(15) Jiang, X.; Su, H.; Shang, W. L.; Zhou, F.; Zhang, Y.; Zhao, W.; Zhang, Q.; Xie, H.; Jiang, L.; Nie, T.; et al. Structure-based development and preclinical evaluation of the SARS-CoV-2 3C-like protease inhibitor simnotrelvir. *Nat. Commun.* **2023**, *14* (1), 6463.
(16) Unoh, Y.; Uehara, S.; Nakahara, K.; Nobori, H.; Yamatsu, Y.; Yamamoto, S.; Maruyama, Y.; Taoda, Y.; Kasamatsu, K.; Suto, T.; Kouki, K.; Nakahashi, A.; Kawashima, S.; Sanaki, T.; Toba, S.; Uemura, K.; Mizutare, T.; Ando, S.; Sasaki, M.; Orba, Y.; Sawa, H.; Sato, A.; Sato, T.; Kato, T.; Tachibana, Y. Discovery of S-217622, a Noncovalent Oral SARS-CoV-2 3CL Protease Inhibitor Clinical Candidate for Treating COVID-19. *J. Med. Chem.* **2022**, *65* (9), 6499−6512.
(17) Huang, C.; Shuai, H.; Qiao, J.; Hou, Y.; Zeng, R.; Xia, A.; Xie, L.; Fang, Z.; Li, Y.; Yoon, C.; Huang, Q.; Hu, B.; You, J.; Quan, B.; Zhao, X.; Guo, N.; Zhang, S.; Ma, R.; Zhang, J.; Wang, Y.; Yang, R.; Zhang, S.; Nan, J.; Xu, H.; Wang, F.; Lei, J.; Chu, H.; Yang, S. A new generation Mpro inhibitor with potent activity against SARS-CoV-2 Omicron variants. *Signal Transduction Targeted Ther.* **2023**, *8* (1), 128.
(18) Allerton, C. M. N.; Arcari, J. T.; Aschenbrenner, L. M.; Avery, M.; Bechle, B. M.; Behzadi, M. A.; Boras, B.; Buzon, L. M.; Cardin, R. D.; Catlin, N. R.; Carlo, A. A.; Coffman, K. J.; Dantonio, A.; Di, L.; Eng, H.; Farley, K. A.; Ferre, R. A.; Gernhardt, S. S.; Gibson, S. A.; Greasley, S. E.; Greenfield, S. R.; Hurst, B. L.; Kalgutkar, A. S.; Kimoto, E.; Lanyon, L. F.; Lovett, G. H.; Lian, Y.; Liu, W.; Martínez Alsina, L. A.; Noell, S.; Obach, R. S.; Owen, D. R.; Patel, N. C.; Rai, D. K.; Reese, M. R.; Rothan, H. A.; Sakata, S.; Sammons, M. F.; Sathish, J. G.; Sharma, R.; Steppan, C. M.; Tuttle, J. B.; Verhoest, P. R.; Wei, L.; Yang, Q.; Yurgelonis, I.; Zhu, Y. A Second-Generation Oral SARS-CoV-2 Main Protease Inhibitor Clinical Candidate for the Treatment of COVID-19. *J. Med. Chem.* **2024**, *67* (16), 13550−13571.
(19) Infectious Diseases Society of America (IDSA). *IDSA Guidelines on the Treatment and Management of Patients with COVID-19*. https://www.idsociety.org/practice-guideline/covid-19-guideline-treatment-and-management/. accessed 21 Febuary 2026.
(20) Hammond, J.; Leister-Tebbe, H.; Gardner, A.; Abreu, P.; Bao, W.; Wisemandle, W.; Baniecki, M. L.; Hendrick, V. M.; Damle, B.; Simón-Campos, A.; Pypstra, R.; Rusnak, J. M. EPIC-HR Investigators. Oral Nirmatrelvir for High-Risk, Nonhospitalized Adults with Covid-19. *N. Engl. J. Med.* **2022**, *386* (15), 1397−1408.
(21) Hashemian, S. M. R.; Sheida, A.; Taghizadieh, M.; Memar, M. Y.; Hamblin, M. R.; Bannazadeh Baghi, H.; Sadri Nahand, J.; Asemi, Z.; Mirzaei, H. Paxlovid (Nirmatrelvir/Ritonavir): A new approach to Covid-19 therapy? *Biomed. Pharmacother.* **2023**, *162*, 114367.
(22) Hu, Y.; Lewandowski, E. M.; Tan, H.; Zhang, X.; Morgan, R. T.; Zhang, X.; Jacobs, L. M. C.; Butler, S. G.; Gongora, M. V.; Choy, J.; Deng, X.; Chen, Y.et al. Naturally occurring mutations of SARS-CoV-2 main protease confer drug resistance to nirmatrelvir. *bioRxiv*. **2022**.
(23) National Institutes of Health (NIH) *COVID-19 Treatment Guidelines*; https://www.covid19treatmentguidelines.nih.gov/management/clinical-management-of-adults/nonhospitalized-adults-therapeutic-management/. accessed 14 November 2025.
(24) Di Santo, R.; Costi, R.; Artico, M.; Ragno, R.; Greco, G.; Novellino, E.; Marchand, C.; Pommier, Y. Design, synthesis and biological evaluation of heteroaryl diketohexenoic and diketobutanoic acids as HIV-1 integrase inhibitors endowed with antiretroviral activity. *Farmaco* **2005**, *60* (5), 409−417.
(25) Johnson, A. A.; Marchand, C.; Patil, S. S.; Costi, R.; Di Santo, R.; Burke, T.; Jr, R. Probing HIV-1 integrase inhibitor binding sites with position-specific integrase-DNA cross-linking assays. *Mol. Pharmacol.* **2007**, *71* (3), 893−901.
(26) Corona, A.; Madia, V. N.; De Santis, R.; Manelfi, C.; Emmolo, R.; Ialongo, D.; Patacchini, E.; Messore, A.; Amatore, D.; Faggioni, G.; Artico, M.; Iaconis, D.; Talarico, C.; Di Santo, R.; Lista, F.; Costi, R.; Tramontano, E. Diketo acid inhibitors of nsp13 of SARS-CoV-2 block viral replication. *Antiviral Res.* **2023**, *217*, 105697.
(27) Madia, V. N.; Emmolo, R.; Patacchini, E.; Amatore, D.; Maloccu, S.; Ialongo, D.; Albano, A.; Ruggieri, G.; Cara, E.; Zarbo, L.; Messore, A.; De Santis, R.; Amoroso, A.; Lista, F.; Esposito, F.; Tramontano, E.; Corona, A.; Di Santo, R.; Costi, R. Structure-Activity Relationships of New 1-Aryl-1H-Indole Derivatives as SARS-CoV-2 Nsp13 Inhibitors. *ChemMedChem* **2025**, *20* (14), No. e202500205.
(28) Albano, A.; Emmolo, R.; De Santis, R.; Patacchini, E.; Madia, V. N.; Maloccu, S.; Ialongo, D.; Ruggieri, G.; Arpacioglu, M.; Scipione, L.; Saccoliti, F.; Amatore, D.; Grilli, G.; Lista, F.; Esposito, F.; Tramontano, E.; Corona, A.; Di Santo, R.; Costi, R. N-alkyl and N-benzyl indoles are anti-SARS-CoV-2 agents and nsp13 inhibitors. *J. Enzyme Inhib. Med. Chem.* **2025**, *40* (1), 2539445.
(29) Saccoliti, F.; Angiulli, G.; Pupo, G.; Pescatori, L.; Madia, V. N.; Messore, A.; Colotti, G.; Fiorillo, A.; Scipione, L.; Gramiccia, M.; Di Muccio, T.; Di Santo, R.; Costi, R.; Ilari, A. Inhibition of Leishmania infantum trypanothione reductase by diaryl sulfide derivatives. *J. Enzyme Inhib. Med. Chem.* **2017**, *32* (1), 304−310.
(30) Madia, V. N.; Nicolai, A.; Messore, A.; De Leo, A.; Ialongo, D.; Tudino, V.; Saccoliti, F.; De Vita, D.; Scipione, L.; Artico, M.; Taurone, S.; Taglieri, L.; Di Santo, R.; Scarpa, S.; Costi, R. D. Synthesis and Biological Evaluation of New Pyrimidine Derivatives as Anticancer Agents. *Molecules* **2021**, *26* (3), 771.

(31) Santos-Martins, D.; Solis-Vasquez, L.; Tillack, A. F.; Sanner, M. F.; Koch, A.; Forli, S. Accelerating AutoDock4 with GPUs and gradient-based local search. *J. Chem. Theory Comput.* **2021**, *17* (2), 1060−1073.
(32) Jin, Z.; Du, X.; Xu, Y.; Deng, Y.; Liu, M.; Zhao, Y.; Zhang, B.; Li, X.; Zhang, L.; Peng, C.; Duan, Y.; Yu, J.; Wang, L.; Yang, K.; Liu, F.; Jiang, R.; Yang, X.; You, T.; Liu, X.; Yang, X.; Bai, F.; Liu, H.; Liu, X.; Guddat, L. W.; Xu, W.; Xiao, G.; Qin, C.; Shi, Z.; Jiang, H.; Rao, Z.; Yang, H. Structure of Mpro from SARS-CoV-2 and discovery of its inhibitors. *Nature* **2020**, *582* (7811), 289−293.
(33) Li, Z.; Gelbaum, C.; Heaner, W. L., IV; Fisk, J.; Jaganathan, A.; Holden, B.; Pollet, P.; Liotta, C. L. Palladium-Catalyzed Suzuki Reactions in Water with No Added Ligand: Effects of Reaction Scale, Temperature, pH of Aqueous Phase, and Substrate Structure. *Org. Process Res. Dev.* **2016**, *20* (8), 1489−1499.
(34) Taglieri, L.; Saccoliti, F.; Nicolai, A.; Peruzzi, G.; Madia, V. N.; Tudino, V.; Messore, A.; Di Santo, R.; Artico, M.; Taurone, S.; Salvati, M.; Costi, R.; Scarpa, S. Discovery of a pyrimidine compound endowed with antitumor activity. *Invest. New Drugs* **2020**, *38* (1), 39−49.
(35) Colotti, G.; Saccoliti, F.; Gramiccia, M.; Di Muccio, T.; Prakash, J.; Yadav, S.; Dubey, V. K.; Vistoli, G.; Battista, T.; Mocci, S.; Fiorillo, A.; Bibi, A.; Madia, V. N.; Messore, A.; Costi, R.; Di Santo, R.; Ilari, A. Structure-guided approach to identify a novel class of anti-leishmaniasis diaryl sulfide compounds targeting the trypanothione metabolism. *Amino Acids* **2020**, *52* (2), 247−259.
(36) Costi, R.; Di Santo, R.; Artico, M.; Massa, S.; Lavecchia, A.; Marceddu, T.; Sanna, L.; La Colla, P.; Marongiu, M. E. Structure−Activity Relationship Studies on Potential Non-Nucleoside DABO-like Inhibitors of HIV-1 Reverse Transcriptase. *Antiviral Chem. Chemother.* **2000**, *11* (2), 117−133.
(37) Duan, Y.; Zhou, H.; Liu, X.; Iketani, S.; Lin, M.; Zhang, X.; Bian, Q.; Wang, H.; Sun, H.; Hong, S. J.; Culbertson, B.; Mohri, H.; Luck, M. I.; Zhu, Y.; Liu, X.; Lu, Y.; Yang, X.; Yang, K.; Sabo, Y.; Chavez, A.; Goff, S. P.; Rao, Z.; Ho, D. D.; Yang, H. Molecular mechanisms of SARS-CoV-2 resistance to nirmatrelvir. *Nature* **2023**, *622* (7982), 376−382.
(38) Kovalevsky, A.; Aniana, A.; Ghirlando, R.; Coates, L.; Drago, V. N.; Wear, L.; Gerlits, O.; Nashed, N. T.; Louis, J. M. Effects of SARS-CoV-2 Main Protease Mutations at Positions L50, E166, and L167 Rendering Resistance to Covalent and Noncovalent Inhibitors. *J. Med. Chem.* **2024**, *67* (20), 18478−18490.
(39) Esler, M. A.; Shi, K.; Rollie, J. A.; Delgado, R.; Vishwakarma, J.; Dabrowska, A.; Prahlad, J.; Moghadasi, S. A.; Harris, R. S.; Aihara, H. Structural basis for varying drug resistance of SARS-CoV-2 Mpro E166 variants. *mBio* **2025**, *16* (7), No. e0262424.
(40) Tan, H.; Chi, X.; Deng, X.; Wang, J. Characterization of the Cross-Resistance of SARS-CoV-2 Main Protease Inhibitors, Ibuzatrelvir, Ensitrelvir, and Nirmatrelvir. *ACS Pharmacol. Transl. Sci.* **2026**, *9* (2), 404−413.
(41) Neilsen, G.; Lan, S.; Slack, R. L.; Lorson, Z. C.; Emanuelli Castaner, A.; Lee, R.; Edwards, K. G.; Zhang, H.; Lee, J.; Cantara, W. A.; Cilento, M. E.; Zhang, H.; De, R.; Amblard, F.; Tedbury, P. R.; Kirby, K. A.; Schinazi, R. F.; Sarafianos, S. G. Strategy to overcome a nirmatrelvir resistance mechanism in the SARS-CoV-2 nsp5 protease. *Sci. Adv.* **2025**, *11* (23), No. eadv8875.
(42) Hamidi, H.; Lilja, J.; Ivaska, J. Using xCELLigence RTCA Instrument to Measure Cell Adhesion. *Bio-Protocol.* **2017**, *7* (24), No. e2646.
(43) Paulis, A.; Onali, A.; Vidalain, P. O.; Lotteau, V.; Jaquemin, C.; Corona, A.; Distinto, S.; Delogu, G. L.; Tramontano, E. Identification of new benzofuran derivatives as STING agonists with broad-spectrum antiviral activity. *Virus Res.* **2024**, *347*, 199432.
(44) Fumagalli, V.; Di Lucia, P.; Ravà, M.; Marotta, D.; Bono, E.; Grassi, S.; Donnici, L.; Cannalire, R.; Stefanelli, I.; Ferraro, A.; Esposito, F.; Pariani, E.; Inverso, D.; Montesano, C.; Delbue, S.; Perlman, S.; Tramontano, E.; De Francesco, R.; Summa, V.; Guidotti, L. G.; Iannacone, M. Nirmatrelvir treatment of SARS-CoV-2-infected mice blunts antiviral adaptive immune responses. *EMBO Mol. Med.* **2023**, *15* (5), No. e17580.
(45) Kuzikov, M.; Costanzi, E.; Reinshagen, J.; Esposito, F.; Vangeel, L.; Wolf, M.; Ellinger, B.; Claussen, C.; Geisslinger, G.; Corona, A.; Iaconis, D.; Talarico, C.; Manelfi, C.; Cannalire, R.; Rossetti, G.; Gossen, J.; Albani, S.; Musiani, F.; Herzog, K.; Ye, Y.; Giabbai, B.; Demitri, N.; Jochmans, D.; Jonghe, S.; Rymenants, J.; Summa, V.; Tramontano, E.; Beccari, A. R.; Leyssen, P.; Storici, P.; Neyts, J.; Gribbon, P.; Zaliani, A. Identification of Inhibitors of SARS-CoV-2 3CL-Pro Enzymating Activity Using a Small Molecule in Vitro Repurposing Screen. *ACS Pharmacol. Transl. Sci.* **2021**, *4* (3), 1096−1110.
(46) Noske, G. D.; de Souza Silva, E.; de Godoy, M. O.; Dolci, I.; Fernandes, R. S.; Guido, R. V. C.; Sjö, P.; Oliva, G.; Godoy, A. S. Structural basis of nirmatrelvir and ensitrelvir activity against naturally occurring polymorphisms of the SARS-CoV-2 main protease. *J. Biol. Chem.* **2023**, *299* (3), 103004.
(47) *Schrödinger Suite, version 2025−1; Protein Preparation Wizard, LigPrep, Jaguar, Desmond, Simulation Interaction Diagram*; Schrödinger, LLC: New York, NY, 2025.
(48) *PyMOL Molecular Graphics System, version 2.4.2*; Schrödinger, LLC: New York, NY, 2020.

https://doi.org/10.1021/acsinfecdis.6c00583
ACS Infect. Dis. XXXX, XXX, XXX−XXX